Supplementary materials

S1.1 Governing equations

In this study, the flow and heat transfer processes within NDASC were assumed to be in a steady state, and the nanofluid flow was turbulent. The realizable k-ε two-equation turbulence model [1] was employed in this paper, with the governing equations presented as follows [2].

Continuity equation:

$$\frac{\partial(\rho u_i)}{\partial x_i}=0 \tag{1}$$

Momentum and energy equations:

$$\frac{\partial(\rho u_i u_j)}{\partial x_i}=-\frac{\partial P}{\partial x_i}+\frac{\partial}{\partial x_j}\left[(\mu+\mu_t)\times\left(\frac{\partial u_i}{\partial x_j}+\frac{\partial u_j}{\partial x_i}\right)-\frac{2}{3}(\mu+\mu_t)\frac{\partial u_i}{\partial x_i}\delta_{ij}-\rho\overline{u'u'_j}\right] \tag{2}$$

$$\frac{\partial\left(\rho u_i T\right)}{\partial x_i}=\frac{\partial}{\partial x_i}\left(\frac{\mu}{\mathrm{Pr}}+\frac{\mu_t}{\mathrm{Pr_t}}\right)\frac{\partial T}{\partial x_i}+Q_{gen} \tag{3}$$

Equation of turbulent kinetic energy k:

$$\frac{\partial\left(\rho u_i k\right)}{\partial x_i}=\frac{\partial}{\partial x_i}\left(\left(\mu+\frac{\mu_t}{\sigma_k}\right)\frac{\partial k}{\partial x_i}\right)+\Gamma-\rho\varepsilon \tag{4}$$

Equation of turbulent energy dissipation ε:

$$\frac{\partial\left(\rho u_i \varepsilon\right)}{\partial x_i}=\frac{\partial}{\partial x_i}\left(\left(\mu+\frac{\mu_t}{\sigma_\varepsilon}\right)\frac{\partial \varepsilon}{\partial x_i}\right)+c_1\Gamma\varepsilon-\rho c_2\frac{\varepsilon^2}{k+\sqrt{v\varepsilon}} \tag{5}$$

The turbulent kinetic energy Γ in equation (6), is defined as:

$$\Gamma=-\overline{u_i u_j}\frac{\partial u_i}{\partial x_i}=\mu_t\left(\frac{\partial u_i}{\partial x_j}+\frac{\partial u_j}{\partial x_i}\right)\frac{\partial u_i}{\partial x_i} \tag{6}$$

The variables ρ, u, P, and T in the equation represent the nanofluid's density, velocity components, pressure, and temperature. At the same time, μ and Pr denote the viscosity and Prandtl number of the nanofluid. μ_t represents the turbulent viscosities, Pr_t, σ_k and σ_ε correspond to the turbulent Prandtl numbers associated with T, k, and ε. Additionally, Q_{gen} signifies the impact of volumetric heating on the working medium caused by incident solar radiation, acting as the source term in Eq. (4).

This study used ANSYS Fluent 2021 R1 based on the finite volume method (FVM) to perform numerical simulations. The governing equations were discretized using a second-order upwind scheme, and the coupling between velocity and pressure was achieved by implementing the SIMPLE algorithm. Furthermore, an enhanced wall treatment technique was applied to capture surface gradients inside and outside the absorber. The discrete ordinate radiation model was used to simulate solar radiation and radiative heat transfer.

The thermal properties of Syltherm-800 thermal oil were expressed by the following equation [3], where the thermal oil temperature is given in K.

$$\rho_{\mathrm{oil}}=-6.0616\times10^{-4}T^2-4.1535\times10^{-1}T+1.1057\times10^3 \tag{7}$$

$$c_{\mathrm{p,oil}}=1.7080T+1.1078\times10^3 \tag{8}$$

$$\lambda_{\mathrm{oil}}=-5.7534\times10^{-10}T^2-1.8752\times10^{-4}T+1.9002\times10^{-1} \tag{9}$$

$$\mu_{\mathrm{oil}}=6.6720\times10^{-13}T^4-1.5660\times10^{-9}T^3+1.3882\times10^{-6}T^2-5.5412\times10^{-4}T+8.4866\times10^{-2} \tag{10}$$

S1.2 Discrete ordinates radiation model

The discrete ordinate radiation model (DORM) considers the radiative transfer equation (RTE) in the $\vec{s}$ direction as a field equation [4, 5].

$$\nabla\cdot\left[I_{\lambda}(\vec{r},\ \vec{s})\vec{s}\right]+(\sigma_{\lambda}+\alpha_{\lambda})I_{\lambda}(\vec{r},\ \vec{s})=\sigma_{\lambda}n^{2}I_{b\lambda}+\frac{\alpha_{\lambda}}{4\pi}\int_{0}^{4\pi}I_{\lambda}(\vec{r},\ \vec{s})\Phi(\vec{s}\cdot\vec{s}')\mathrm{d}\Omega \tag{11}$$

where I_{λ} represents the radiative intensity, which is a function of the Cartesian coordinate system $\vec{r}=(x,y,z)$ in the domain and the direction of the beam, $\vec{s}=(s_x,s_y,s_z)$. σ_{λ}, n, and α_{λ} correspond to the spectral absorption coefficient, refractive index, and scattering coefficient, respectively. These parameters characterize the medium's optical properties concerning solar radiation. Additionally, λ, $\overrightarrow{s'}$, $d\Omega$, Φ, and $I_{b\lambda}=\sigma T^4/\pi$ denote the wavelength, scattering direction vector, solid angle, phase function, and blackbody intensity derived from the Planck function, respectively. The symbol σ represents the Stefan-Boltzmann constant (5.67×10^{-8} kg/($s^3\cdot K^4$)). Formula (12) encompasses the rate of change of incident radiation intensity (the first term on the left-hand side of the equation), the absorbed radiation (the second term on the left-hand side of the equation), the emitted radiation (the first term on the right-hand side of the equation), and the scattered radiation (the second term on the right-hand side of the equation).

The incident radiation spectrum was divided into N wavelength bands in the non-gray DORM. Within each wavelength interval, integration of the RTE was performed to derive the transport equation for $I_{\lambda}\Delta\lambda$, which represents the contained radiation energy in the spectral band $\Delta\lambda$. Assumptions were made that each specified wavelength band exhibits gray body radiation. The emissions from the black body within each band were formulated as follows:

$$E_b(\lambda,T)=\left[F(0\rightarrow n\lambda_2 T)-F(0\rightarrow n\lambda_1 T)\right]n^2 I_{b\lambda} \tag{12}$$

where In $F(0\rightarrow n\lambda T)$ represents the proportion of radiation energy from the black body within the wavelength range of 0 to λ; T and n correspond to the temperature and refractive index of the medium, respectively. The number of wavelength bands can be adjusted to achieve the desired solution accuracy. Finally, the total intensity $I_{\lambda}(\vec{r},\vec{s})$ denotes the sum of radiative intensities across all bands and in all directions $\vec{s}$ at a specific position $\vec{r}$.

$$I_{\lambda}(\vec{r},\vec{s})=\sum_k I_{\lambda_k}(\vec{r},\vec{s})\Delta\lambda_k$$

(13)

S1.3 Parameter definitions

The definition of Reynolds number (*Re*), average heat transfer coefficient (*h*), average Nusselt number (*Nu*), friction factor (*f*), and Q_{gen} is as follows [6]:

$$\mathrm{Re}=\frac{\rho u d}{\mu} \tag{14}$$

$$h=q_w\big/\left(T_w-T_f\right) \tag{15}$$

$$Nu=\frac{hd}{\lambda} \tag{16}$$

$$f=\frac{2\Delta P_L d}{\rho u^2} \tag{17}$$

where T_f represents the nanofluid's volumetric temperature, while ρ, μ and λ correspond to the nanofluid's density, viscosity, and thermal conductivity, respectively. q_w and T_w denote the average heat flux and the average temperature on the inner tube, respectively. d represents the inner diameter of the inner tube, and ΔP_L signifies the pressure drop per unit distance in the flow direction. Lastly, u represents the average velocity of the nanofluid and is defined as follows:

$$u = \frac{4M}{\rho \pi d^2} \tag{18}$$

where M is the mass flow rate of the nanofluid.

The heat gain Q_u of the nanofluid is defined as:

$$Q_u = M \cdot c_{p,oil} \cdot \left(T_{out} - T_{in}\right) \tag{19}$$

Q_{gen} in expression (3) is defined as:

$$Q_{gen} = Q_{SR} - Q_{OL} - Q_{TR} \tag{20}$$

where Q_{SR} is the solar radiation, Q_{OL} is the optical radiation loss, and Q_{TR} is the thermal radiation loss, presented as follows.

$$\begin{aligned} Q_{SR} &= \Delta\lambda \int_{\vec{s}\cdot\vec{n}>0} I_{in,\lambda} \vec{s} \cdot \vec{n} d\Omega \\ &= \int_{\vec{s}\cdot\vec{n}>0} I_i \vec{s} \cdot \vec{n} d\Omega \end{aligned} \tag{21}$$

$$Q_{OL} = \left(1 - \varepsilon_g\right) Q_{SR} \tag{22}$$

$$Q_{TR} = \varepsilon_g E_b\left(\lambda, T\right) \tag{23}$$

In Eq. (22), $I_{in,\lambda}$ represents the radiation intensity for the solar wavelength range (300−2500 nm). The vector $\vec{n}$ denotes the normal direction of the surface. When $\vec{s} \cdot \vec{n} > 0$, the radiation flux is considered to be directed inward towards the surface. Furthermore, Eq. (21) allows one to obtain the total solar radiation intensity, I_i, resulting in the modified expression in the denominator of Eq. (22). Since Eq. (24) deals with the thermal radiation flux, the values of λ_1 and λ_2 in $E_b(\lambda, T)$ are chosen within the infrared wavelength range [4]. The thermal efficiency η of the NDASC is defined as follows [7]:

$$\eta = \frac{Q_u}{A_a \cdot DNI} \tag{24}$$

where A_a is the aperture area of the collector.

S1.4 Boundary conditions

The boundary conditions used in this study are as follows:

1) A no-slip condition was applied at the interface between the solid and fluid.

2) The mass flow rate at the inlet of the nanofluid was 0.7 kg/s, and the outlet was set as a pressure outlet.

3) The glass tubes' inner and outer surfaces were considered semitransparent walls. The emissivity (ε_g) of the glass tubes was set to 0.86 [8].

4) The outer surface of the glass cover was subjected to a mixed boundary of convective and radiative heat transfer, and the heat transfer rate to the surroundings was calculated using the following equation:

$$q = h_{co}\left(T_{co} - T_a\right) + \varepsilon_g \sigma \left(T_{co}^4 - T_s^4\right) \tag{25}$$

5) T_{co} represents the temperature of the outer surface of the glass cover, T_a denotes the ambient temperature, which was set to 298 K in this study, and T_s represents the sky temperature, which was 8 K lower than T_a [9]. The coefficient of convective heat transfer, denoted as h_{co}, was assumed to be a constant value of 10 W/(m^2·K).

S1.5 Grid independence test and model validation

Grid independence test

To address the impact of grid quantity on numerical results, we conducted simulations for a specific case with T_{in}=600 K and an absorption coefficient (AC) of 80 m^{-1}. Five simulations were carried out, each with a different grid quantity. The outcomes and corresponding grid models are presented in Figures 2(a) and (b). As the grid numbers increased from 6988335 to 12534080, we observed a relative variation in f of less than 1.5%, while the relative variation in thermal efficiency remained below 0.02%. Therefore, we utilized a grid system of 6988335 cells for the simulation to strike an optimal balance between computational time and accuracy.

Model validation

The accuracy of the heat transfer and flow models for indirect absorption solar collectors (IASCs) was verified with the Gnielinski equation for Nu and the Petukhov equation for [32]. Figure 2(c) compares the numerical simulation results with the correlation equations for Nu and f, with the mean errors controlled within 6.3% and 4.3%, respectively. These findings suggest that the developed CFD model is reliable for heat transfer and flow modeling.

Numerical simulations were carried out with the DASC experiments of XU et al [42] with the same operating conditions to validate the model's accuracy further. As illustrated in Figure 2(d), the mean error of the thermal efficiency was less than 2.7%, suggesting that the developed model also exhibits reliable accuracy in modeling radiative transport.

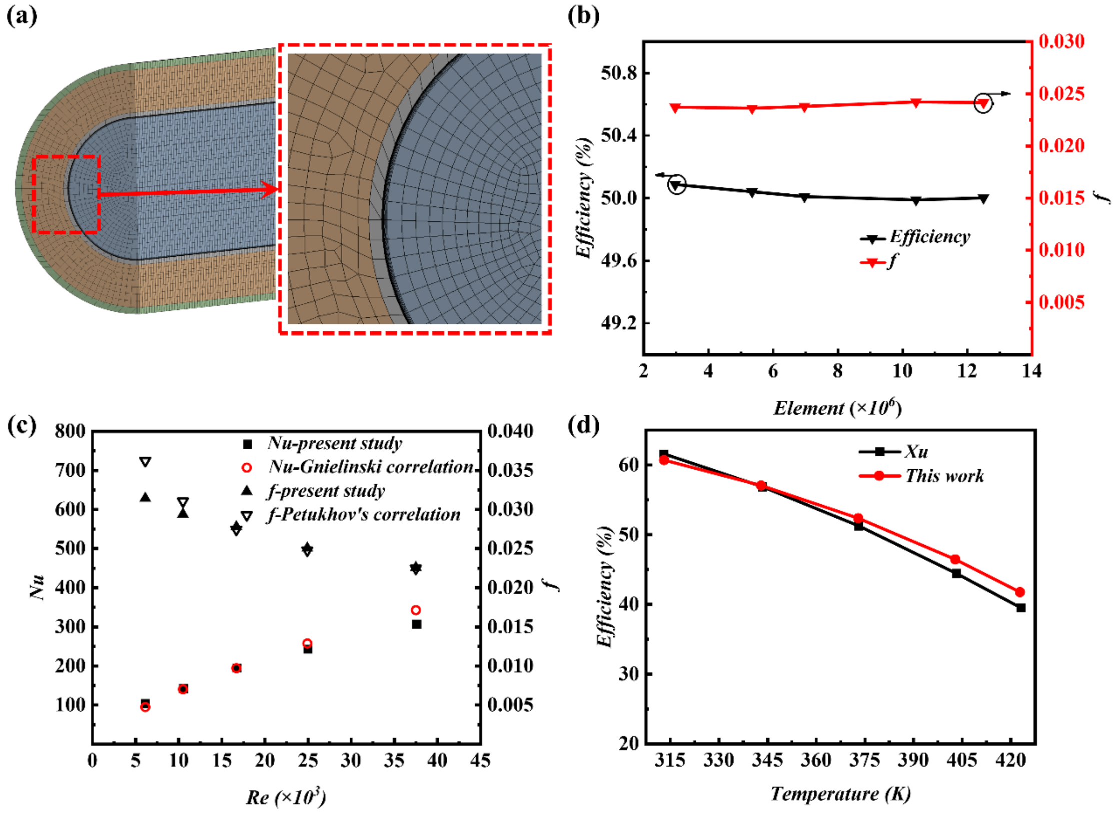

Figure S1 (a) Grid generation; (b) Grid independence test; (c-d) Model validation

Table S1 Geometrical and thermal parameters of the NDASC

Parameters	Value	Parameters	Value
Collector tube length, L/m	7.8	Glass emissivity [8] (ε_g)	0.86
Absorption tube inner diameter, d_{ai}/mm	66	Glass transmittance [8, 10] (T_g)	0.94
Absorption tube outer diameter, d_{ao}/mm	70	Glass density/(kg·m^{-3})	2230
Glass cover inner diameter, d_{ci}/mm	109	Glass thermal conductivity/(W·(m·K)$^{-1}$)	1.2 W/(m·K)
Glass cover outer diameter, d_{co}/mm	115	Syltherm-800 mass flow rate/(kg·s^{-1})	0.7 kg/s

Table S2 Optical parameters of the coatings

Coating type	Solar transmittance/%	Infrared reflectance/%	Solar absorbance/%
Sn-In_2O_3 [11]	84.6	87	—
ZnO [12]	66.2	81.2	—
TiO_2/Ag/TiO_2 [11]	41	98	—
WTi-Al_2O_3 [13]	—	97	92

Table S3 Coverage angles of heat mirrors at different inlet temperatures

Inlet temperature/K	Coating coverage angle θ_1/(°)
400	−106− −180/106−180
450	−102− −180/102−180
500	−98− −180/98−180
550	−90− −180/90−180
600	−180–180

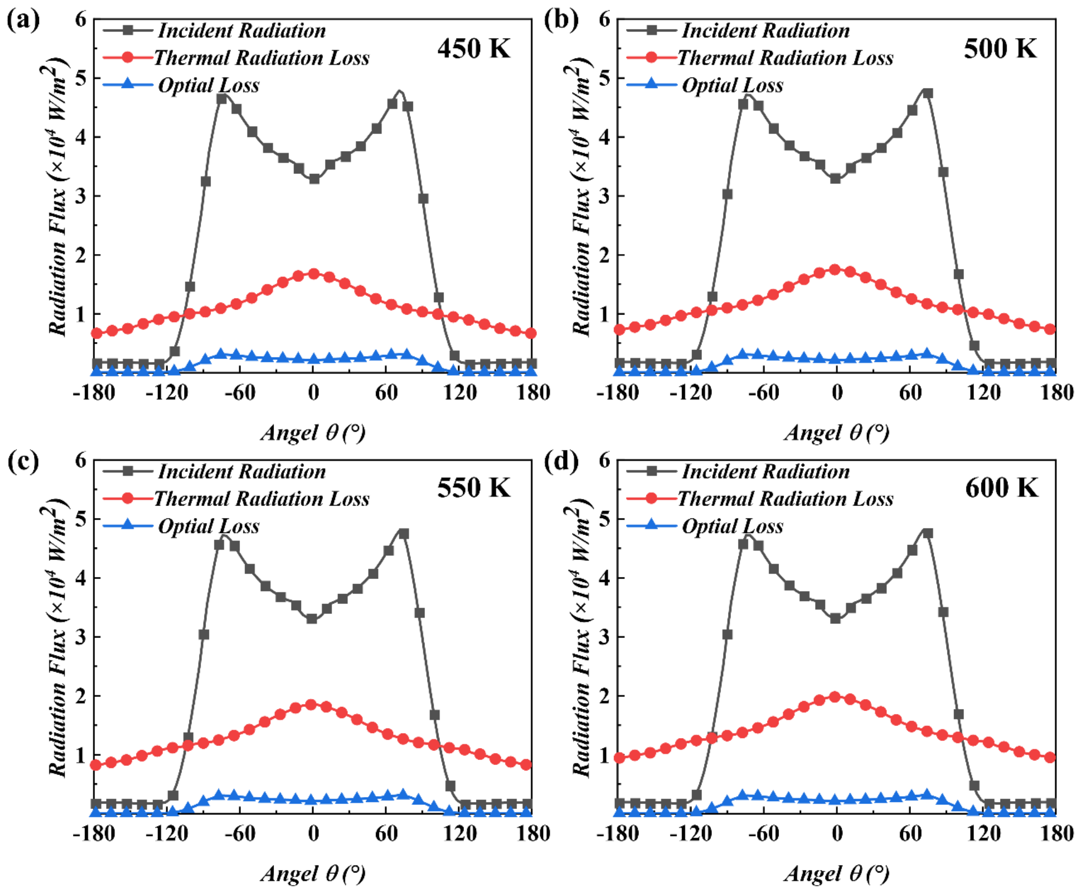

Figure S2 (a−d) Energy flow distribution curves of the collector tube with T_{in}=450−600 K

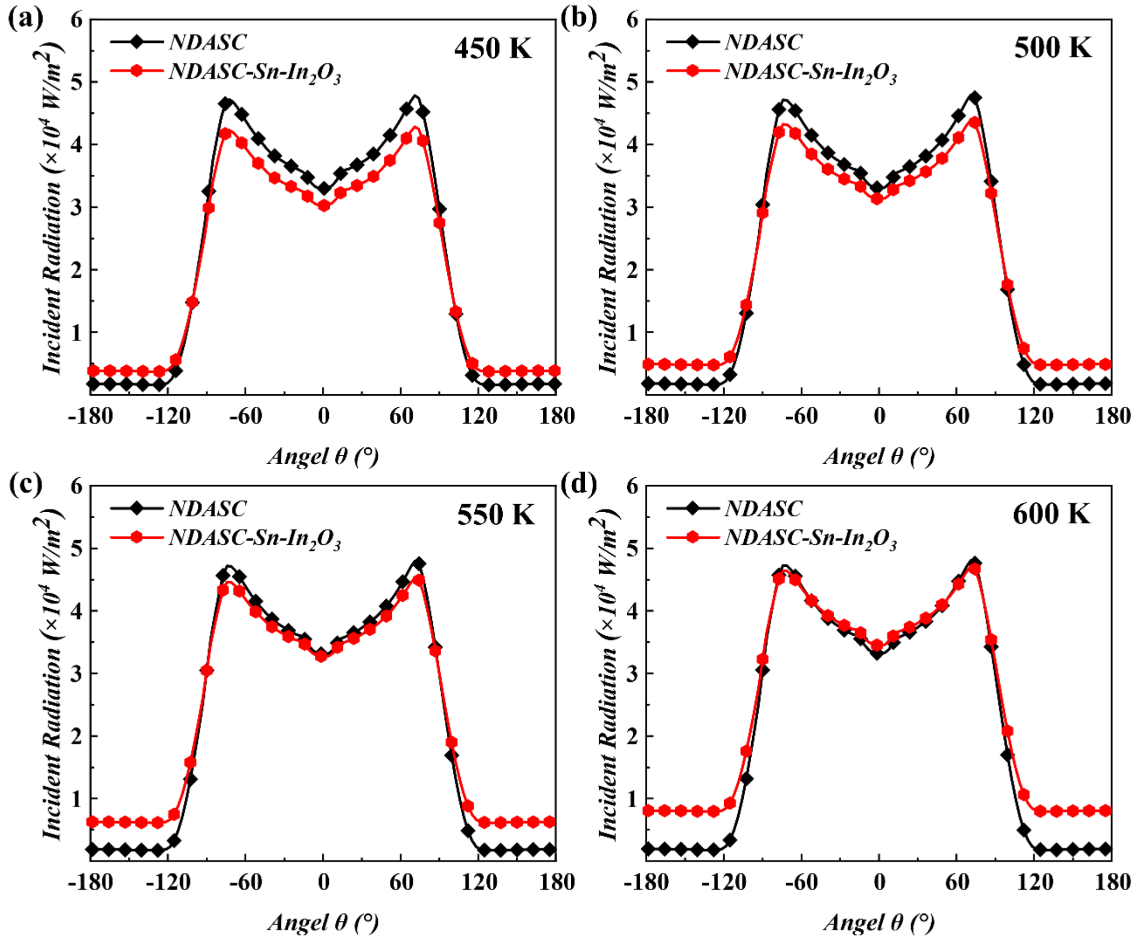

Figure S3 (a−d) Energy flow distribution curves of the NDASC with global Sn-In_2O_3 coatings at T_{in}=450−600 K

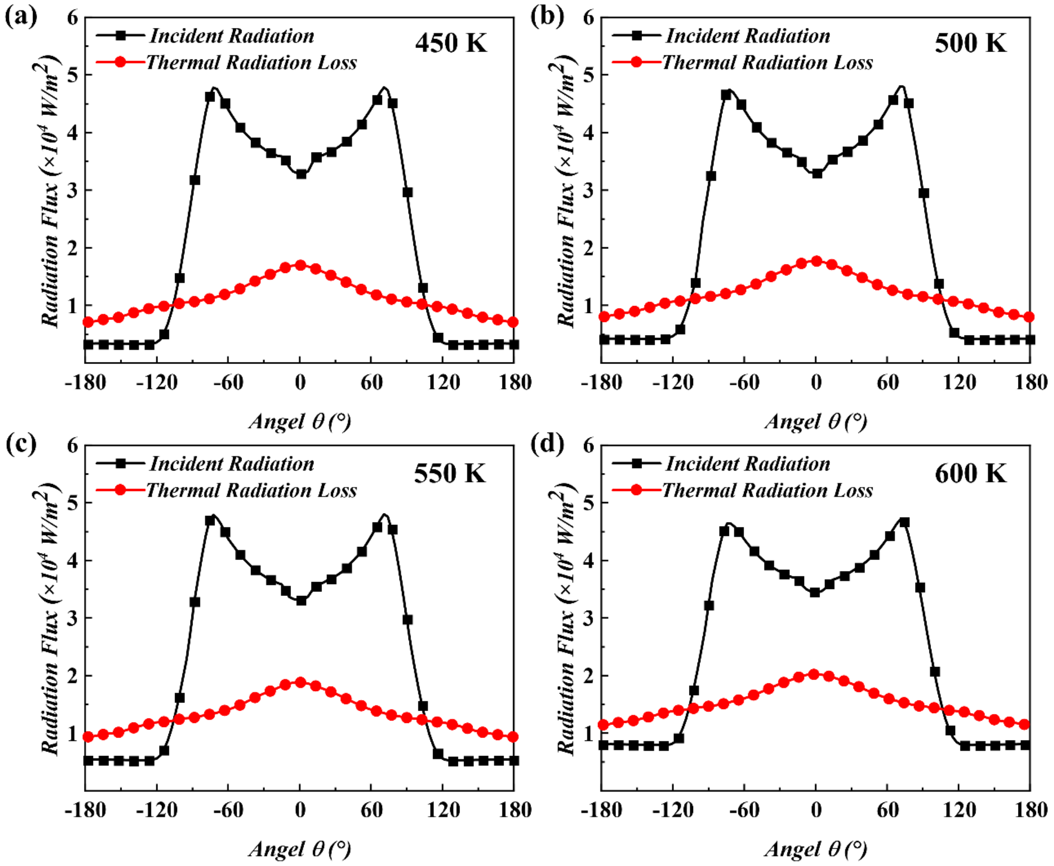

Figure S4 (a−d) Energy flow distribution curves of the NDASC with local Sn-In_2O_3 coatings at T_{in}=450−600 K

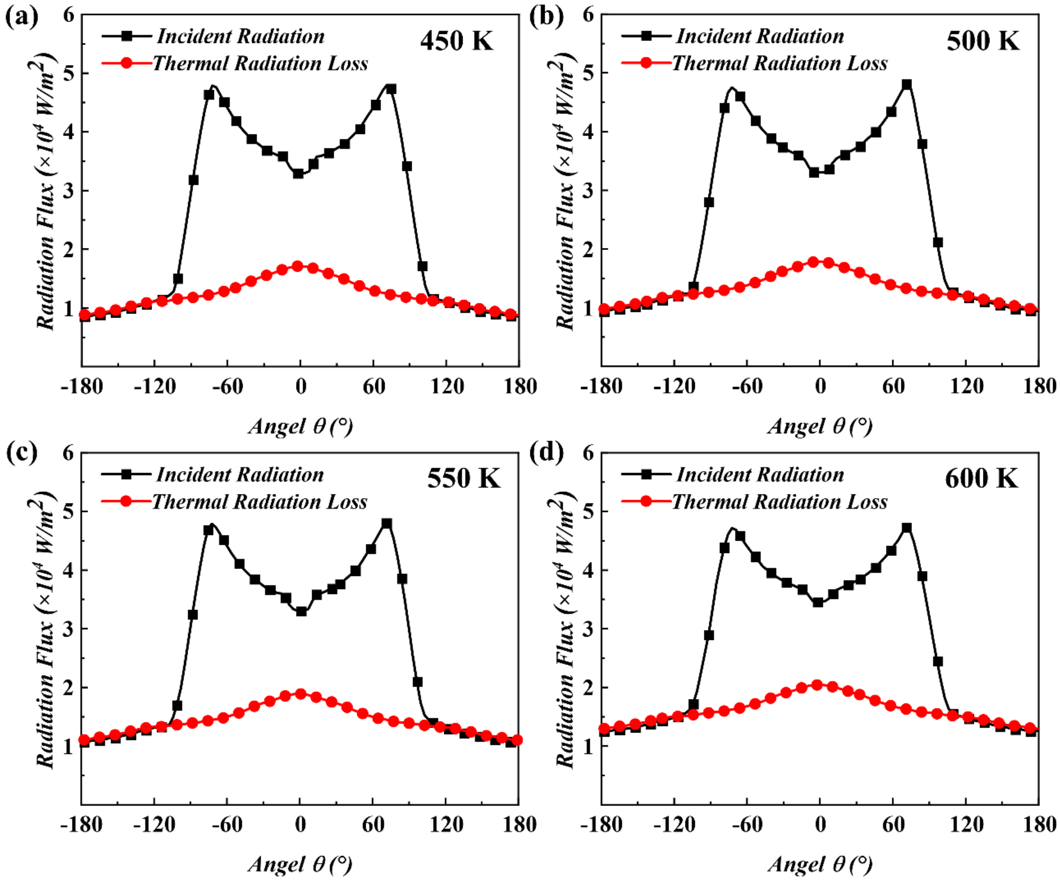

Figure S5 (a−d) Energy flow distribution curves of the NDASC with local thermal mirror/reflection coatings at T_{in}=450−600 K

References

[1] LIU Peng, ZHENG Nian-ben, LIU Zhi-chun, et al. Thermal-hydraulic performance and entropy generation analysis of a parabolic trough receiver with conical strip inserts [J]. Energy Conversion and Management, 2019, 179: 30−45. DOI:10.1016/j.enconman.2018.10.057.

[2] SHIH T H, LIOU W W, SHABBIR A, et al. A new k-ϵ eddy viscosity model for high Reynolds number turbulent flows [J]. Computers & Fluids, 1995, 24(3): 227−238. DOI: 10.1016/0045-7930(94)00032-T.

[3] ZHU Xiao-wei, ZHU Lei, ZHAO Jing-quan. Wavy-tape insert designed for managing highly concentrated solar energy on absorber tube of parabolic trough receiver [J]. Energy, 2017, 141: 1146−1155. DOI: 10.1016/j.energy.2017.10.010.

[4] INC A. ANSYS Fluent Theory Guide [M]. ANSYS, 2021.

[5] MAADI S R, KHATIBI M, EBRAHIMNIA-BAJESTAN E, et al. Coupled thermal-optical numerical modeling of PV/T module–Combining CFD approach and two-band radiation DO model [J]. Energy Conversion and Management, 2019, 198: 111781. DOI: 10.1016/j.enconman.2019.111781.

[6] LIU Peng, DONG Zhi-min, LV Jin-yi, et al. Numerical study on thermal-hydraulic performance and exergy analysis of laminar oil flow in a circular tube with fluid exchanger inserts [J]. International Journal of Thermal Sciences, 2020, 153: 106365. DOI: 10.1016/j.ijthermalsci.2020.106365.

[7] JARAMILLO O A, BORUNDA M, VELAZQUEZ-LUCHO K M, et al. Parabolic trough solar collector for low enthalpy processes: An analysis of the efficiency enhancement by using twisted tape inserts [J]. Renewable Energy, 2016, 93: 125−141. DOI: 10.1016/j.renene.2016.02.046.

[8] FAN Man, LIANG Hong-bo, YOU Shi-jun, et al. Heat transfer analysis of a new volumetric based receiver for parabolic trough solar collector [J]. Energy, 2018, 142: 920−931. DOI: 10.1016/j.energy.2017.10.076.

[9] FORRISTALL R. Heat Transfer Analysis and Modeling of a Parabolic Trough Solar Receiver Implemented in Engineering Equation Solver [R]. Colorado: National Renewable Energy Laboratory, 2003. DOI: 10.2172/15004820

[10] CHENG Z D, HE Y L, CUI F Q, et al. Comparative and sensitive analysis for parabolic trough solar collectors with a detailed Monte Carlo ray-tracing optical model [J]. Applied Energy, 2014, 115: 559−572. DOI: 10.1016/j.apenergy.2013.11.001.

[11] KHULLAR V, TYAGI H, OTANICAR T P, et al. Solar selective volumetric receivers for harnessing solar thermal energy [J]. Journal of Heat Transfer, 2018, 140(6): 062702. DOI: 10.1115/1.4039214.

[12] SINGH N, KHULLAR V. Experimental and theoretical investigation into effectiveness of ZnO based transparent heat mirror covers in mitigating thermal losses in volumetric absorption based solar thermal systems [J]. Solar Energy, 2023, 253: 439−452. DOI: 10.1016/j.solener.2023.02.057.

[13] WANG Xiao-yu, GAO Jun-hua, HU Hai-bo, et al. High-temperature tolerance in WTi-Al_2O_3 cermet-based solar selective absorbing coatings with low thermal emissivity [J]. Nano Energy, 2017, 37: 232−241. DOI: 10.1016/j.nanoen.2017.05.036.